

ACCEPTED MANUSCRIPT

Wire, hybrid, and laser-cut X-pinch as Talbot-Lau backlighters for electron density diagnostics

To cite this article before publication: Maria Pia Valdivia Leiva *et al* 2022 *Plasma Phys. Control. Fusion* in press <https://doi.org/10.1088/1361-6587/ac4b95>

Manuscript version: Accepted Manuscript

Accepted Manuscript is “the version of the article accepted for publication including all changes made as a result of the peer review process, and which may also include the addition to the article by IOP Publishing of a header, an article ID, a cover sheet and/or an ‘Accepted Manuscript’ watermark, but excluding any other editing, typesetting or other changes made by IOP Publishing and/or its licensors”

This Accepted Manuscript is © 2022 IOP Publishing Ltd.

During the embargo period (the 12 month period from the publication of the Version of Record of this article), the Accepted Manuscript is fully protected by copyright and cannot be reused or reposted elsewhere.

As the Version of Record of this article is going to be / has been published on a subscription basis, this Accepted Manuscript is available for reuse under a CC BY-NC-ND 3.0 licence after the 12 month embargo period.

After the embargo period, everyone is permitted to use copy and redistribute this article for non-commercial purposes only, provided that they adhere to all the terms of the licence <https://creativecommons.org/licenses/by-nc-nd/3.0>

Although reasonable endeavours have been taken to obtain all necessary permissions from third parties to include their copyrighted content within this article, their full citation and copyright line may not be present in this Accepted Manuscript version. Before using any content from this article, please refer to the Version of Record on IOPscience once published for full citation and copyright details, as permissions will likely be required. All third party content is fully copyright protected, unless specifically stated otherwise in the figure caption in the Version of Record.

View the [article online](#) for updates and enhancements.

Wire, Hybrid, and Laser-cut X-pinch as Talbot-Lau Backlighters for Electron Density Diagnostics

M. P. Valdivia^{1,2}, G. W. Collins IV^{1*}, F. Conti¹ and F. N. Beg¹

¹Center for Energy Research, University of California San Diego, La Jolla, California 92093, USA

²Department of Physics and Astronomy, Johns Hopkins University, Baltimore, Maryland 21218, USA

*Now at General Atomics, Inertial Fusion Technology, San Diego, California 92121, USA

E-mail: mpvaldivialeiva@ucsd.edu

Received xxxxxx

Accepted for publication xxxxxx

Published xxxxxx

Abstract

Talbot-Lau X-ray Deflectometry (TXD) enables refraction-based imaging for high-energy-density physics (HEDP) experiments, and thus, it has been studied and developed with the goal of diagnosing plasmas relevant to Inertial Confinement and Magnetic Liner Inertial Fusion. X-pinch, known for reliably generating fast (~ 1 ns), small (~ 1 μm) x-ray sources, were driven on the compact current driver GenASIS (~ 200 kA, 150 ns) as a potential backlighter source for TXD. Considering that different X-pinch configurations have characteristic advantages and drawbacks as x-ray generating loads, three distinct copper X-pinch configurations were studied: the wire X-pinch, the hybrid X-pinch, and the laser-cut X-pinch. The Cu K-shell emission from each configuration was characterized and analyzed regarding the specific backlighter requirements for an 8 keV TXD system: spatial and temporal resolution, number of sources, time of emission, spectrum, and reproducibility. Recommendations for future experimental improvements and applications are presented. The electron density of static objects was retrieved from Moiré images obtained through TXD. This allowed to calculate the mass density of static samples within 4% of the expected value for laser-cut X-pinch, which were found to be the optimal X-pinch configuration for TXD due to their high reproducibility, small source size (≤ 5 μm), short duration (~ 1 ns FWHM), and up to 10^6 W peak power near 8 keV photon energy. Plasma loads were imaged through TXD for the first-time using laser-cut X-pinch backlighting. Experimental images were compared with simulations from the X-ray Wave-Front Propagation code, demonstrating that TXD can be a powerful x-ray refraction-based diagnostic for dense Z-pinch loads. Future plans for Talbot-Lau Interferometry diagnostics in the pulsed-power environment are described.

Keywords: x-pinch, x-ray backlighters, x-ray deflectometry, Talbot-Lau interferometry

1. Introduction

Pulsed x-ray sources are widely used in imaging diagnostics that probe, amongst other parameters, the density distribution, size, and dynamics of dense, transient objects such as those found in a variety of High Energy Density

(HED) plasmas and warm dense matter [1]–[4]. A few objects are of special interest to the HED community, such as laser-driven shock dynamics, pulsed-power wire-array implosions, and the growth of Rayleigh–Taylor unstable features in Inertial Confinement Fusion (ICF) capsules [3], [5], [6]. In these systems, the probing x-ray source must be adequately

bright, short (temporally), small (spatially), and ideally exhibit a narrow photon energy bandwidth. For example, properly characterizing the in-flight implosion of an ICF capsule requires an x-ray pulse duration ≤ 1 ns, while to resolve small features in cold, dense ICF fuel at peak compression [7] or characterize uncoated or coated liners in Magnetic Liner Fusion (MagLIF) [8], [9], <10 μm sources are necessary.

High-contrast imaging of HED experiments requires x-ray source spectra to meet specific conditions. Generally, in these experiments, matter is opaque to visible and extreme ultraviolet (XUV) light, as well as x-rays <1 keV, and therefore requires probing photons in the range of 1-100 keV [10]. The x-ray backlighter brightness must be larger than that expected from the plasma to be imaged, at least in the spectral bandwidth used to image the object. In this way, the negative impact on effective resolution due to data noise can be mitigated by high system throughput and photon yield. Moreover, x-ray backlighter flux requirements are specific to each experiment and should consider vacuum chamber geometry and the characteristics of object to be diagnosed. For example, a 4×25 μm Mo wire X-pinch driven by the XP generator (450 kA, 45 ns) emitted 1-3 keV soft x-rays of ~ 1 mJ (≤ 1 ns duration) with sufficient flux to produce high contrast radiographs of a fruit bug with object magnification of 3-5x and object-to-detector distance of 10-30 cm [11].

Historically, a variety of x-ray backlighting imaging diagnostics have been employed in HED experiments, including high-resolution monochromatic x-ray imaging systems such as point-projection and pinhole cameras [3], [11]–[14], Kirkpatrick–Baez microscopes [15], [16], Fresnel zone plates [17], [18], and spherically bent crystal systems [19], [20]. Typically, these diagnostics measure attenuation, however, when probing low-Z matter with ~ 1 -100 keV x-rays, the amount that the light is refracted is much more than the amount that is absorbed [21], as seen in Figure 1 from Ref. [21]. Thus, a diagnostic utilizing refractive processes will deliver significantly higher contrast owing to higher phase-effects when compared to standard attenuation-based radiography. In combination with micron source sizes, refraction-based x-ray imaging diagnostics can characterize tens of microns to millimeter sized objects with micrometer spatial resolution, providing electron density diagnostic capabilities through phase retrieval. This motivates the development and implementation of an imaging diagnostic that makes use of x-ray refraction. To this end, the Talbot-Lau X-ray Deflectometer (TXD) has shown to be a powerful diagnostic based on phase-contrast imaging methods that can provide refraction information in addition to attenuation [22]. It has been demonstrated that TXD can map elemental composition [23] as well as detect the presence of microstructures by making use of small-angle scattering effects [24], [25]. Talbot Interferometry, including TXD diagnostic methods, are described in detail in the next section.

Frequently, the aforementioned diagnostics make use of x-ray sources produced by driving a high-intensity ($I > 10^{15}$ W/cm²) sub-nanosecond laser pulse into a solid target, which can generate plasmas with conversion efficiencies of $<40\%$ [26], [27], producing bright, short-duration x-ray pulses useful for characterizing HED experiments via x-ray backlighting [28]–[30]. Recent experiments at the Laboratory for Laser Energetics have demonstrated the feasibility of laser-generated x-ray sources for TXD diagnostics. Experiments performed in the Multi-TeraWatt laser ($\sim 10^{15-16}$ W/cm²) recently demonstrated increased ~ 5 -10 μm spatial resolution and experiments on the Omega EP laser ($\sim 10^{16-17}$ W/cm²) delivered >10 μm spatial resolution. However, backlighter target modification leading to increased spatial resolution has shown to negatively impact signal-to-noise ratio as well as TXD image contrast [31]. A new TXD monochromatic configuration uses a multi-layer mirror to only reflect 8 keV emission. This configuration has been implemented and tested in the laboratory using broadband emission from a tungsten rotating anode medical x-ray tube. MTW and Omega EP monochromatic TXD experiments seeking to demonstrate increased TXD image contrast and high spatial resolution are underway. As an alternative, a pulsed-power Z-pinch configuration [32]–[34] known as an X-pinch can produce x-ray sources (≤ 1 ns, ~ 1 μm) that can achieve the spatial resolution required for TXD diagnostics [35]. Perhaps more importantly, X-pinch can be generated using compact, portable, and increasingly efficient current drivers with the potential for coupling to other experiments, as well as being placed in the current return path of a higher current driver, enabling single-system, in-situ source driving and target production with little detriment to the performance of either [4], [36]–[38]. Using small-scale generators, the spatial, temporal, and spectral characteristics of X-pinch sources can be optimized at reduced cost.

X-pinch are traditionally composed of two or more thin wires, crossed at mid-length to form an ‘X’, placed between the electrodes of a pulsed power current driver. A large (tens to thousands of kA), fast-rising (generally ≥ 1 kA/ns) current is driven through the wires. The entirety of the driver current flows through the cross point of the X (as compared to the individual legs of the X), creating a localized maximum $\mathbf{J} \times \mathbf{B}$ ($\propto I^2/r^2$, where ‘I’ is the current and ‘r’ is the pinch radius), which forms a ‘micro z-pinch’, that ultimately develops instabilities and collapses, leading to a very hot (~ 1 keV), dense (10^{22} ions/cm³), localized (~ 1 μm), and strongly emitting plasma region. This ‘hot spot’ emits radiation characteristic of a thermal plasma. During or subsequent to this collapse, non-thermal fast electrons produce additional line radiation sources that have a significantly higher percentage of hard x-rays than the emission from the hot spot and are typically less localized and longer in duration [33], [34]. X-pinch sources have been used to produce radiographic

images of other Z-pinch plasmas and several studies have characterized X-pinch plasmas with respect to x-ray sources, electron beams, and plasma jets [33], [34], [39]–[41], among other aspects.

In this paper, studies of x-ray emission from X-pinch loads driven by a compact current driver are presented. The emission of each X-pinch configuration studied was evaluated and their suitability as x-ray backlighter for Talbot-Lau X-ray Deflectometry (a refraction-based electron density diagnostic) was determined. This paper is organized as follows: Section 2 describes Talbot interferometry and specifies the diagnostic capabilities of Talbot-Lau X-ray Deflectometry in context to its adaptation to the HEDP environment. Section 3 presents the experimental set up used to study and compare x-ray emission from three distinct X-pinch configurations as well as the diagnostics used to characterize the emission. Section 4 shows emission diagnostic results for each X-pinch configuration and evaluates their x-ray backlighting performance for Talbot-Lau diagnostics. Moiré images of static solid objects obtained with each X-pinch configuration are shown and object electron density is calculated for selected images. Optimal X-pinch configuration for x-ray backlighting is determined and Moiré images of plasma objects are shown and compared to simulations.

2. Talbot-Lau X-ray Interferometry

Talbot interferometry [42]–[45] is a refraction-based imaging technique that takes advantage of the near-field diffraction of a coherent, monochromatic plane wave as it passes through a periodic diffraction grating. This image is repeated at regular distances away from the grating plane, also known as the Talbot length and the repeated images are called self-images or Talbot images. A second grating is placed at a multiple of the Talbot length thus turning phase variations into intensity changes that can be projected onto a detector. Talbot interferometers have been used in many fields including biomedical [46]–[49], and material science [50], [51] applications. In standard Talbot interferometry configurations, phase, attenuation, and scatter information is obtained through phase-stepping techniques, where objects are exposed to multiple x-ray pulses for time periods of the order of seconds. In contrast, to properly diagnose HED experiments, a Talbot interferometer should produce a diagnostic image using a single, short (nanosecond or less) x-ray pulse. This can be achieved in the deflectometry mode, where a Moiré pattern is created by adding a small rotation ($\sin\theta \approx \theta$) between gratings. The probing beam phase changes produced by refractive index changes within an object can be retrieved by measuring fringe shifts in the Moiré pattern [52]–[55]. Furthermore, a variation of the Talbot Interferometer, called a Talbot-Lau interferometer, allows for non-coherent illumination by adding an additional micro-grating, thus creating an array of

quasi-coherent sources [42], [49], [56]–[59]. Therefore, Talbot-Lau X-ray Deflectometry (TXD) has been made available to diagnose HED plasma experiments using standard x-ray backlighters [21].

In Talbot interferometry, phase change is proportional to the refraction angle α produced by the probed object, electron density gradient ∇n_e can be calculated from the following equation:

$$\alpha(x, y) = \frac{1}{n_c} \frac{\partial}{\partial x} \int n_e(x, y, z) dz \quad (1)$$

where ' n_c ' is the critical density (which depends on probing beam wavelength ' λ ') and ' n_e ' is the electron density in the object.

In the Moiré mode [43], [60], [61], the total probing beam refraction angle ' α ' produced by a sample object is equivalent to the fringe shift scaled by the effective angular resolution of the interferometer, W_{eff} . When the object is placed between the g_0 and g_1 gratings (Figure 1, top), $W_{\text{eff}} = g_0/p$, with g_0 the period of the source grating and ' p ' the distance between the object and g_0 . When the object is placed between g_1 and g_2 (Figure 1, bottom), $W_{\text{eff}} = g_2/q$, with g_2 the period of the analyzer grating and ' q ' the distance between the object and g_2 [62]. It is worth noting that, in addition to object placement relative to the gratings, the electron density gradient dynamic range depends on the probing x-ray energy (since critical density is inversely proportional to λ^2), Talbot order, and grating periods. Additionally, the minimum fringe shift value that can be measured in a Moiré image also impacts electron density retrieval accuracy, as it is determined by the system spatial resolution and Moiré fringe contrast [22].

When developing and implementing TXD in the HED plasma environment, one must consider the probing energy required, grating period, vacuum chamber dimensions, and potential target locations with respect to Talbot-Lau inter-grating distances (' L ' and ' d ' in Figure 1) [63]. The location of the object being probed must be chosen considering that its location with respect to the gratings will determine system effective angular resolution [44], [62] in addition to dictating object magnification which in turn impacts spatial resolution. Typically, if a laser-produced backlighter is used to illuminate the interferometer, a large Talbot magnification translates to better angular and spatial resolution [21]. Furthermore, although restrictions of maximum length should be considered, higher Talbot orders are preferred as they provide a narrower energy bandwidth (see Figure 4, discussed later) [42]. Given that Talbot distances depend on grating periods, the interferometer is flexible enough to accommodate the diversity of HED experiment scales by simply varying grating period and location. Considering that the x-ray source size required to characterize HED experiments is ideally $<10 \mu\text{m}$, the Talbot-Lau Interferometer presented here uses a $2.4 \mu\text{m}$ period source grating so that imaging spatial resolution matches the radiographic resolution.

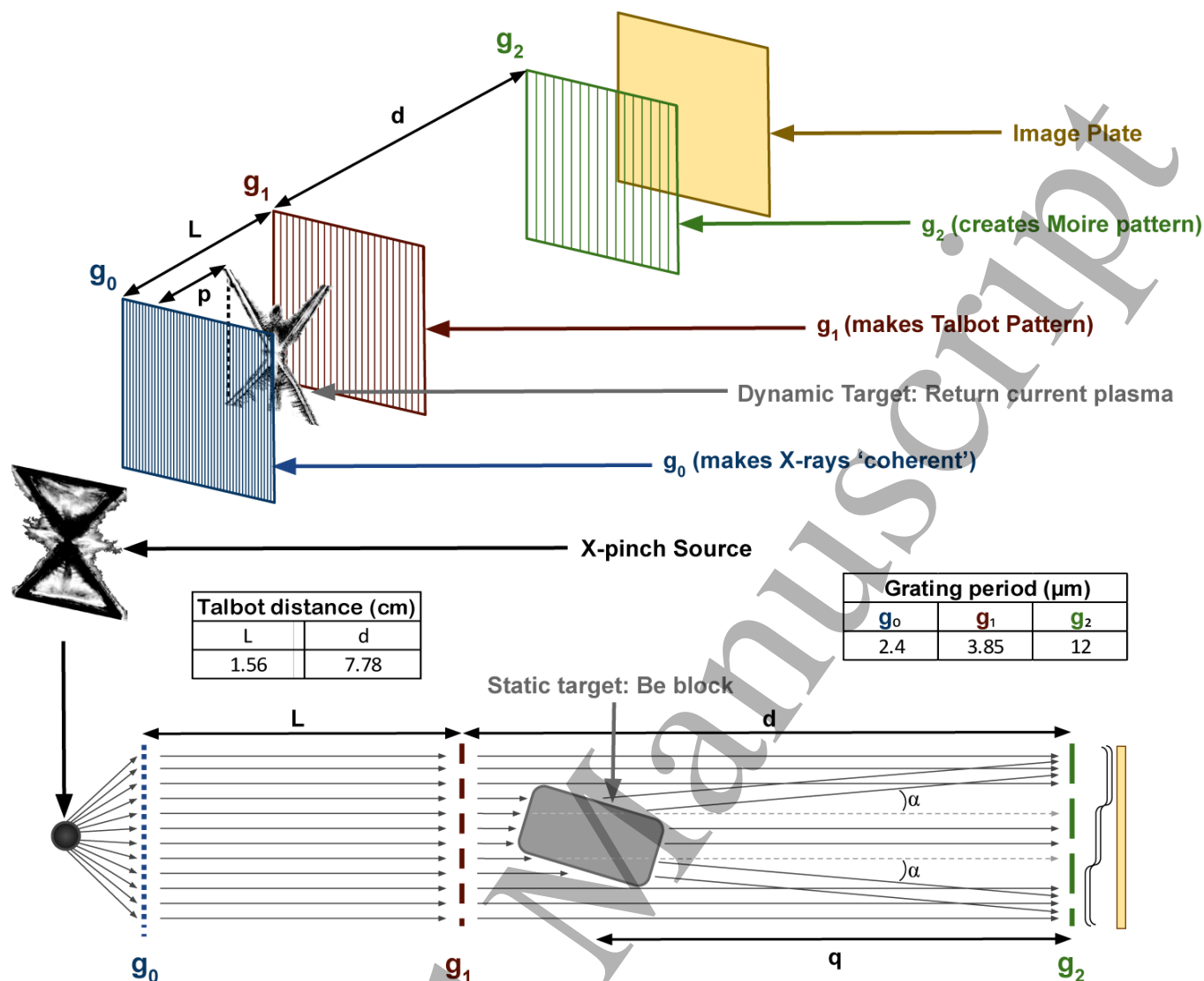


Figure 1. Talbot-Lau Interferometer configurations used on GenASIS. Talbot order $m=1$ with $L = 1.56$ cm and $d = 7.78$ cm. Grating periods of: $2.4 \mu\text{m}$ for source grating g_0 , $3.85 \mu\text{m}$ for phase grating g_1 , and $12.0 \mu\text{m}$ for analyser grating g_2 . The three-dimensional figure (top) shows the setup for probing a ‘Dynamic target’, which is a non-pinching X-pinch placed in between g_0 and g_1 , replacing a current return post. The two-dimensional schematic (bottom) shows the ‘Static target’ configuration used to probe a Be slab of $1 \times 1 \times 0.5 \text{ cm}^3$ placed just after g_1 .

If the object symmetry is known, absolute local electron density can be obtained. In the case of axial symmetry, Abel inversion can deliver a 3D map of local electron density. If the object shape is unknown (or rather no symmetry assumptions can be made), a simple integration along the refraction angle detection axis can be made, thus delivering the electron density integrated along the line-of-sight. In similarity to most other interferometry techniques, a reference image is required to determine Moiré fringe shifts. To enable single-shot HED experiments characterization, Moiré reference images can be obtained through ex-situ phase-stepping [64]. Furthermore, Fourier enables attenuation information retrieval, in addition to refraction [22]. These signals can be combined, delivering elemental composition (Z-average) information [23], which makes TXD a versatile and powerful diagnostic technique. In

the HED adaptations [65], [66], Talbot-Lau diagnostic timing is given by the x-ray backlighter pulse duration and spatial resolution is limited by the backlighter source size, similar to other transmission-based techniques [67], [68].

3. Experimental setup

3.1 GenASIS current driver

The **Generator for Ablation Structure and Implosion Studies**, or GenASIS, at UCSD, is a compact, low-inductance current driver, with a typical peak current of ~ 200 kA, over a 150 ns quarter-period. This current signal is shown in Figure 2 below:

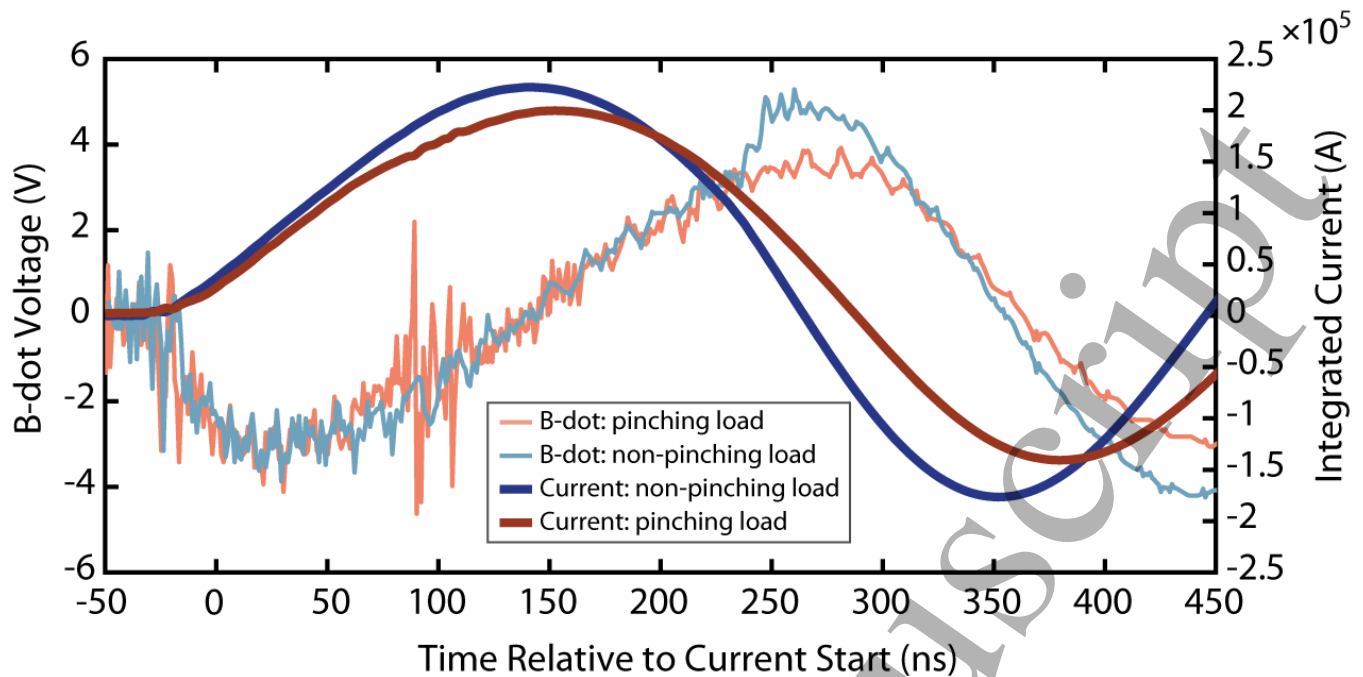


Figure 2: Raw B-dot signals (in volts, on the left y-axis) from a short-circuit (non-pinching: thin blue line) and an X-pinch (pinching: thin orange line) load, and corresponding integrated current signals (thick blue and orange lines, in Amperes, on the right y-axis). The pinch is clearly visible in the orange dI/dt (B-dot) signal, where sharp peaks are visible. Slight dips in the matching current profile are also visible. Note that, for pinching loads on GenASIS, the peak current is slightly lower, and the rise-time is slightly longer.

Twelve 20 nF capacitors are divided into blocks of 3, each block with its own low-inductance multi-gap switch bank, and charged to 72 – 75 kV, for a total of 620 – 700 J of stored energy. A built-in -70 kV trigger Marx bank, charged along with the capacitors via a voltage divider, breaks the switches. The current flows directly from the capacitors into a coaxial-conical power feed and into the load. B-dot probes monitor the current before and after the target load [69], [70]. GenASIS is well-suited to benchmark the TXD diagnostic as its drive parameters (peak current and rise-time) are comparable not only to the increasing number of compact current generators being built, but also to those of X-pinch placed in current return paths for higher-current generators [71]–[74].

3.2 X-pinch x-ray backlighters

X-ray emission from three types of X-pinch configurations - wire [39], [75] (WXP), hybrid [76], [77] (HXP), and laser-cut [78], [79] (LCXP) - was systematically studied to determine the optimal x-ray backlighting source for Talbot-Lau X-ray Deflectometry. WXPs are composed by a set of crossed thin wires (few to hundreds of microns) in the shape of an 'X' (Figure 3a), as described above in Section 1. HXP use a single thin wire to bridge the gap (few millimeters) between two conical electrodes (Figure 3b). In the case of LCXP, thin foils are machined in the shape of an 'X' (Figure 3c), where the thickness of the legs decreases from base to mid-point, effectively reducing the total area (and thus mass)

of the cross point. Recent studies found that x-ray emission from WXP varies with linear mass and wire count and originates from separate pinch (hot-spot) and electron-beam-driven sources, while HXP emission originates from single or co-located sources and is the configuration most sensitive to the driver current profile. In turn, LCXP emission was found to be the brightest and smallest [31]. Most of the X-pinch studied used copper to obtain ~8 keV K-shell emission, though a few HXPs were tested using Constantan, a high-resistivity Ni-Cu alloy.

Different sub-configurations of each X-pinch type were tested, using the same brass load electrodes (see Figure 3) spaced by ~12 mm. The configurations tested were:

- Wire X-pinch (WXP) of 2x18, 2x25, 4x18, 4x25, and 2x50 μm diameter Cu wires, (where the first number refers to the number of legs in the X-pinch, and the second number is the wire diameter) all with an opening angle of $\sim 35^\circ$ (see Figure 3a).
- Hybrid X-pinch (HXP) of 25 μm diameter Cu or Constantan (45% Ni - 55% Cu alloy) wire between Mo conical electrodes. Some Cu HXPs had 45 μm of polyimide film wrapped around the anode cone to prevent early-time, low driver current from ablating the wire cross-point. Optimal spacing between conical electrodes was ≤ 2.5 mm (shown in Figure 3b). Further details about

distance parameter optimization can be found in a separate publication [31].

- Laser-cut X-pinch (LCXP) machined from 25 and 30 μm thick annealed or hardened temper copper foil with an average cross-point width of $\sim 25 \mu\text{m}$ (see Figure 3 c). The foils were cut using a TRUMPF Trumark 5000 laser workstation with a target design similar to that found in Refs. [31], [78], [79].

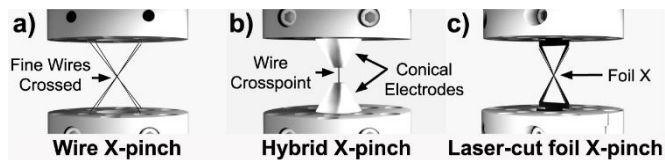


Figure 3: Computer Aided Design (CAD) images of the a) Wire, b) Hybrid, and c) Laser-cut foil X-pinch studied. All configurations had the same brass electrode clearance. Other key features are labelled in the individual frames.

The Talbot-Lau diagnostic platforms implemented on GenASIS were designed using a set of 8 keV gratings: source grating (g_0) of 2.4 μm period, a phase grating (g_1) of 3.85 μm period, and an analyzer grating (g_2) of 12 μm period [22], [65]. To fit the platform inside the vacuum chamber, a Talbot order of $m=1$ was chosen, thus $L = 1.6 \text{ cm}$ and $d = 7.8 \text{ cm}$. A contrast curve for the TXD interferometer setup used here is plotted as a function of energy in Figure 4 (right y-axis).

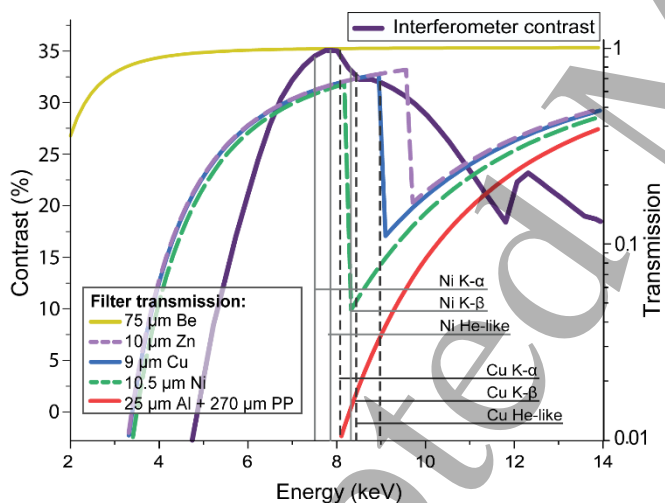


Figure 4. Interferometer contrast curve for GenASIS TXD platforms along with Cu and Ni x-ray emission expected from the X-pinch loads studied.

The interferometer quality is affected by the maximum contrast between bright and dark field signal in the phase-curve [24], [42]. In TXD, interferometer contrast is defined as $C = (I_{\text{max}} - I_{\text{min}}) / (I_{\text{max}} + I_{\text{min}})$, where $I_{\text{max, min}}$ are the maximum and minimum intensity value, respectively. Contrast was computed considering grating parameters and includes the

geometrical broadening of the Talbot pattern by the finite source grating openings [80]. Emission from the X-pinch configurations described is expected to be primarily line radiation in the 8-9 keV range for copper and nickel [10], [41], [65], [79], [81], [82]. It is worth noting that narrower contrast curves can be obtained by setting up the interferometer using higher Talbot orders, but the vacuum chamber geometry did not allow in the present experiments.

Two object target types were probed in these experiments. The first was a static solid object: a Be slab of $0.5 \times 2.5 \times 5.0 \text{ mm}^3$, set at a small angle $< 2^\circ$ to obtain constant x-ray refraction at the edges and no refraction at the center. The second was a dynamic plasma load, where X-pinch of $4 \times 25 \mu\text{m}$ Al, $2 \times 25 \mu\text{m}$ Cu, or $2 \times 25 \mu\text{m}$ W wires were placed on the return current path of GenASIS and received $\leq 50\%$ of the total current, hence, they ablated but did not pinch.

In the dynamic plasma TXD configuration (Figure 1, top), another 45 μm Kapton layer protected the phase-grating return-post X-pinch. The Moiré images were recorded using Fujifilm BAS-SR image plates, which were placed behind the analyzer grating rotation stage, producing an object magnification of $\sim 2 \times$. The image plates were protected from stray light by wrapping them in 12.5 μm aluminum foil. The “static target” Be slab was placed between g_1 and g_2 (Figure 1, bottom). The source grating (g_0) was placed such that the TXD platform viewed the cross-point in the middle of the field of view, $\sim 4.5 \text{ cm}$ away from the X-pinch, resulting in effective angular resolution $W_{\text{eff}} = 199 \mu\text{rads}$. A 45 μm Kapton filter was used to protect the source grating against ablation, material deposition, or deformation due to thermal expansion from the X-pinch backlighter.

The plasma x-ray emission parameters of the source X-pinch (as opposed to the return-post X-pinch) were diagnosed with a variety of tools. Emission timing/duration and flux/integrated-energy information was obtained using a set of 6 Si-PIN diodes with a sensitive area of either 0.28 or 1.00 mm^2 and a rise-time of 700 ps [83]. The diodes were filtered using Ross-pairs [84] to determine the relative x-ray flux emitted in specific energy ranges - namely for the Cu K-shell range (10.5 μm Ni, 9 μm Cu, 10 μm Zn, and 25 μm Al + 270 μm polypropylene) and lower energies. Transmission curves for these filters are shown in Figure 4 (left y-axis). Si-PIN diodes have a well-defined responsivity (A/W) at specific photon energy ranges, enabling calculation of the peak flux and total energy/photon count emitted from the X-pinch within the Ross-pair-determined energy ranges. The diode-scope system has a temporal resolution of 1-2 ns.

A flat Highly-Ordered Pyrolytic Graphite (HOPG) spectrometer [85] captured Cu (and Ni) K-shell spectra ($\sim 8000 - 9200 \text{ eV}$) which is the emission relevant for the Talbot-Lau setup used here. The HOPG spectrometer was filtered with 15 μm Kapton to protect the crystal and has a spectral resolution of $E/\Delta E \sim 30$. All spectra were recorded

with Fujifilm BAS-SR image plates which were filtered with $10\ \mu\text{m}$ Aluminum to block stray light.

A slit-wire array consisting of a combination of filtered slits and a set of micron size wires placed across the slit provided one dimensional, radiographic source-size information. The size of the x-ray source is determined from the size of the shadow, or penumbra cast by the wires in the array, and the magnification at the imaging plane for the diagnostic [86]. Different filters, including Be, Al, Al+polyimide, Ti, Fe, and Ni were used to determine the source size of cold $K\alpha$, and hotter (He or H-like) emitting regions. The high-Z wires used, which had various diameters to estimate source size, included $150, 18, 10, 7.5,$ and $5\ \mu\text{m}$ W, 75 and $13\ \mu\text{m}$ Mo, $50\ \mu\text{m}$ Cu, and $25\ \mu\text{m}$ Ni-Cu. The slit-wire array was placed $\sim 15\ \text{cm}$ from the X-pinch source. The radiography image was recorded with a Fujifilm BAS-TR image plate ($25\ \mu\text{m}/\text{pixel}$), placed $\sim 15\ \text{cm}$ from the wires, achieving a magnification of $\sim 1x$. Considering the resolution of the image plates, this slit-wire diagnostic cannot truly resolve the $5\text{-}10\ \mu\text{m}$ wires, meaning source-size determinations in this range are estimates.

2. Talbot-Lau X-ray Deflectometry performance in the pulsed-power environment

4.1 X-ray Backlighter source analysis

While backlighter source characterization for these experiments involved testing a variety of configurations for each X-pinch type (wire, hybrid, or laser-cut), only the arrangements of each type that produced the best sources for use in the TXD experiments will be presented. More in-depth information about the performance of the different X-pinch sources on GenASIS is available in Ref. [31]. The results described in the subsequent paragraphs are presented in Figure 5, which gives K-shell flux and temporal data obtained from the $9\ \mu\text{m}$ Cu filtered Si-PIN diode (Figure 5a), the Cu/Ni K-shell source size via the Ni-filtered penumbral slit-wire array (Figure 5b), and the K-shell spectrum via the HOPG crystal spectrometer (Figure 5c).

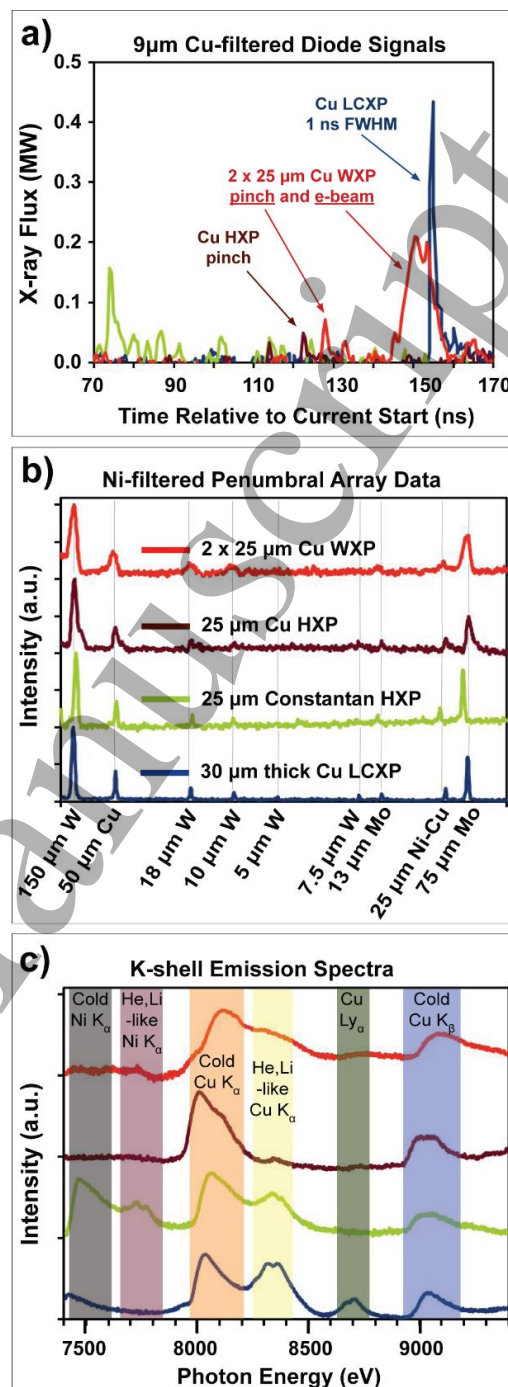


Figure 5. Plots showing x-ray source (Cu K-shell) data for $2 \times 25\ \mu\text{m}$ Cu WXP (red line), $25\ \mu\text{m}$ Cu HXP (dark red lines), $25\ \mu\text{m}$ Constantan HXP (light green lines), and LCXP (blue lines). a) Lineouts from the Ni-filtered penumbral slit-wire array with wires labelled below. The exaggerated width of the wires in the WXP plot pertains to a spatially separated electron beam source. LCXP is the only one that captures the $5\ \mu\text{m}$ W wire. b) K-shell emission spectra with key transitions highlighted. Cold $K\alpha$ and $K\beta$ refer to emission from Ne-like or lesser-ionized ions. c) Signals from an Si-PIN diode filtered with $9\ \mu\text{m}$ Cu showing calculated photon flux (not transmission adjusted) as a function of time relative to GenASIS current start. The lack of hard x-ray flux from typical $25\ \mu\text{m}$ Cu HXP, and the temporally separated pinch and e-beam signal in the $2 \times 25\ \mu\text{m}$ Cu WXP are clearly visible.

Recall that a variety of Cu wire X-pinchs (WXP) were tested in these studies including 2x18, 2x25, 4x18, 4x25, and 2x50 μm configurations. The 2x50 μm WXP did not pinch, while 2x18 and 4x18 μm WXP pinched too early (well before peak current) in the current drive, and with variable results. 2x25 and 4x25 μm Cu WXP pinched reliably, however the former (2x25 μm) produced slightly better emission considering TXD backlighting purposes [35]. Data from these 2x25 μm Cu WXP are shown as red lines in Figure 5. Emission (in the ~ 8 keV energy range) from the 2x25 μm WXP (Figure 5a), typically occurred in two separate peaks. The first was a shorter (1-2 ns FWHM), lower flux (0.1 - 0.2 MW) peak occurring on average, at 122 ± 4 ns after current start, characteristic of the hot pinch/collapse source. Between 4-40 ns later, a second, longer (2-20 ns FWHM), higher flux (≥ 0.2 MW) peak occurs, characteristic of the electron-beam generated source described in Sec. I. Typical HXR source size for the WXP is presented in Figure 5b, showing the penumbra of wires as small as 10 μm . However, the WXP penumbra are clearly similar in size to the larger 50–150 μm penumbra, due to a combination of multiple exposures (from the two peaks seen in Figure 5a) from a large and/or moving source. As such, we estimate the e-beam generated HXR source from these WXP to be ~ 50 –100 μm in size. It is worth noting that 25% of these 2x25 μm WXP exhibited minimal secondary peaks (in the diode data), and these typically produced penumbra characteristic of a ~ 10 μm HXR source, while 25% generated multiple second, broader peaks with equal or greater amounts of penumbral ‘smearing’ than those WXP with a single peak post-pinch. Also worth noting is that 4x25 μm Cu WXP consistently produced shorter e-beam generated sources (≤ 10 ns FWHM) temporally nearer to the pinch source (≤ 10 ns after), but the penumbral data was consistently poor, indicating ≥ 50 μm HXR sources in all cases.

HXP made of 25 μm Cu (maroon-colored lines in Figure 5) produced single photodiode peaks with relatively low (≤ 0.1 - 0.3 MW) HXR flux, when the conical electrodes were ideally spaced at ~ 2.5 mm, from both insulated and non-insulated electrodes. Emission timing however, differed dramatically between these two cases, with the non-insulated HXP pinching at $\sim 115 \pm 14$ ns after current start, while the insulated Cu HXP pinched at $\sim 135 \pm 7$ ns. Pulse width for the HXR emission averaged 2 ns FWHM. Penumbral data (Figure 5b) for the 25 μm Cu HXP shows evidence of a second HXR source, but the main penumbral peak suggests that the main HXR source is ≤ 7.5 μm . Alternatively, the 25 μm Constantan HXP produced, on average, a single dominant HXR peak (green line in Figure 5a), with ≥ 0.1 MW flux, ~ 2 ns duration at FWHM, and an optimal source size of ≤ 7.5 μm (see Figure 5b). Not shown in Figure 5 are a number of insulated Cu HXP that produced second sources, since this was attributed to the dramatically reduced amount of coronal plasma produced in these two as compared to the non-insulated Cu HXP, which

delayed pinch time, and required additional reduction of the conical electrode spacing to < 2.0 mm.

Representative hard x-ray data for the LCXP (blue line) show a single, higher flux (≥ 0.4 MW), narrow (~ 1 ns FWHM, possibly limited by the diagnostics rise time) peak in Figure 5a that clearly images the 5 μm wire in Figure 5b. Emission timing for the LCXP was 145 ± 17 ns, which is a much larger range of pinch timings than either the wire or the insulated Cu HXP, which likely relates to the variability in linear mass at the cross-point introduced by the laser cutting process.

Time-integrated spectral information in the Ni and Cu K-shell range is presented in Figure 5c for the four X-pinchs thus far discussed, which serves to confirm observations regarding the nature of the photodiode peaks and penumbral images, as well as to offer insight into the plasma conditions that produce these sources. Each spectrum is normalized relative to the minimum and maximum from its respective image plate. All four spectra show a lower energy (~ 8.0 -8.1 keV) Cu K_{α} line (and a corresponding K_{β} line at ~ 9 keV), produced by fast (≥ 10 keV) electrons striking a Ne-like, 30-200 eV Cu plasma on the order of $n_i = 10^{18-19} \text{ cm}^{-3}$. This is the e-beam generated source, present in all configurations, even in Cu HXP and LCXP which clearly only have one dominant HXR diode signal. The observations regarding a large and/or moving HXR source in the penumbral data for the 2x25 μm WXP appear confirmed with the smearing together of the ~ 8.1 and higher energy 8.3-8.4 keV Cu K_{α} lines. Each of the four X-pinchs possesses this higher energy (8.3-8.4 keV) Cu K_{α} line, though it is barely above background noise levels in the Cu HXP case. For the Constantan HXP, and WXP, this line is likely produced by a ~ 1000 eV, $\geq 10\%$ solid density ($n_i \sim 10^{22} \text{ cm}^{-3}$) source, which tends to be predominantly ionized to He and Li-like, consistent with hot pinch plasma conditions in other X-pinch experiments [87]. The much lower-intensity 8.3 keV line in the Cu HXP is either produced by a 0.6-0.8 keV source with $n_i \sim 10^{22} \text{ cm}^{-3}$, or a 1 keV source with $n_i \sim 10^{21} \text{ cm}^{-3}$. Not yet discussed is the highest energy line in the LCXP, at ~ 8.6 keV, present in $> 50\%$ of LCXP spectra, which is characteristic of an H-like Cu plasma and suggests that the LCXP pinch source reaches temperatures of up to 2.0-2.5 keV. The Ni K_{α} lines in the Constantan spectra support the observations inferred from Cu K_{α} lines, as there are both cold (7.5 keV) and hot (~ 7.8 keV) Ni K_{α} lines.

Reviewing the data, beyond a variability in pinch timing, the LCXP clearly produces the optimal source for the TXD diagnostic described above: the highest frequency of single (or co-located within 200 μm) sources, with greater K-shell flux than either HXP or WXP pinch sources. While the total integrated photon count for the WXP e-beam generated sources is typically greater than that produced by the LCXP (since the former emit for a much longer time), these e-beam generated sources are much larger (and potentially moving as well), and thus less than satisfactory for creating Moiré patterns of fine meshes and radiographing micron-scale

objects. Analyzing the photon flux produced by HXPs and LCXPs (and hot pinch sources from WXPs) using the Ross-pair filtered diodes reveals that the ratio of flux for L-shell (~1 keV), continuum (>3 keV), and K-shell (8-9 keV) emission is about 100:10:1. In the case of the LCXP, this represents a total ~8 keV photon count of $\sim 10^{10}$ photons/ns/sr or greater. For comparison, laser-produced Cu K_{α} sources (10 ps) have shown to produce $\sim 10^{11-13}$ photons/pulse/sr [21].

Table 1 below provides a summary of the x-ray emission characteristics (>3 keV) for the main X-pinch configurations analyzed. Average values of x-ray emission peak time are provided with associated error. Owing to the limited data collected, approximate values are listed for HXP. Similarly, x-ray emission intensity is given as a range of values to account for data statistics limitations.

Table 1. Summary of typical x-ray emission values for Wire, Hybrid, and Laser-Cut X-pinch loads studied

	X-pinch material (μm)	Number of peaks	Average peak time (ns) *after current start	Intensity (MW)	Pulse FWHM (ns)	X-ray source FWHM (μm)
WXP	Cu wire: 2x25	2+	122 \pm 4	0.1-0.2	1-2	10 (first peak)
			126-162 \pm 4	0.2	2-20	50-100 (second peak)
HXP	Cu wire : 25	1	$\sim 115 \pm 14$	0.1-0.5	2	≥ 20
	Cu wire: 25 - <i>Insulated</i>	1	135 \pm 7	0.2-0.3		5-20
	Constantan wire: 25	1	82 \pm 9	0.2		≥ 7.5
LCXP	Cu foil: 30	1	145 \pm 17	2-12	1	5-20

4.2 Moiré imaging of static target

Adapting a Talbot-Lau interferometer diagnostic platform to a new experimental environment requires an assessment of a number of factors, most importantly, fringe contrast and grating survival. Regarding the latter, recall that a 45 μm Kapton film protected the grating(s): g_0 for shots with the static Be target, and g_0 and g_1 for the dynamic plasma shots. With this setup, no grating damage was observed for interferometers using either the static solid object or the dynamic plasma object in any of the X-pinch configurations studied. No significant damage was done to the Kapton film either, though it was replaced every few shots due to accumulation of material deposited by the source X-pinch and/or return-post plasma.

Detector characteristics should be considered in Moiré fringe contrast analysis. As Figure 4 indicates, interferometer contrast depends on x-ray backlighter energy and thus, if the detector has a higher gain centered within the maximum of the contrast curve, optimal contrast is achieved. If the emission energy has a significant component of higher energies that can be transmitted through the gold grating bars, then the contrast will be lower due to an increased background signal unless the detector has significantly lower sensitivity to higher energies.

The interferometers were first tested using a rotating copper anode x-ray medical tube of 15 μm FWHM x-ray source with a distinctive emission line at ~8 keV. Moiré images were recorded using an x-ray CCD camera with a rapidly decaying gain for energies >12.5 keV [22]. A fringe contrast of 22-27% was measured (Figure 6a) compared to the 35% contrast obtained in XWFP simulations (Figure 4).

X-ray CCDs are the ideal detector for 8 keV TXD measurements given that their quantum efficiency reaches

70% at this energy level and rapidly decays to 25% at 10 keV and less than 5% above 20 keV. However, x-ray CCDs are susceptible to electromagnetic pulses and noise, making them a less than ideal choice for the pulsed-power environment. While image plates are not affected by electromagnetic pulses, they have significantly higher gain when comparing high (>20 keV) and low (<10 keV) x-ray energies [88], [89].

To evaluate contrast loss due to detector choice, a rough comparison between image plate performance compared to x-ray CCDs can be made considering previous experiments where fringe contrast was measured at 0.5-7% using image plates [35]. This was attributed to detector gain differences and thus, similar lower contrast is expected from all Moiré images recorded with image plates using the X-pinch x-ray sources studied here. The Moiré fringe contrast measured in the results here presented (Figures 6b-e) is consistent with the 0.5-7% measured previously. It is worth noting that BioMAX equivalent x-ray film could be a better alternative to image plates and x-ray CCDs. X-ray film has high gain at lower energies and can provide higher spatial resolution [89]–[95] but it is not susceptible to electronic failure, hence, its performance will be investigated in future studies. Even though x-ray film comes at a higher cost in experimental time and effort when compared to image plates, it is important to note that maximizing gain at the interferometer design energy will increase signal-to-noise ratio, which has been shown beneficial to fringe contrast maximization [85], in addition to providing better detector resolution ($\sim 0.12 \pm 0.03 \mu\text{m}$) [83].

Moiré fringe formation was demonstrated with x-ray backlighting from most X-pinch configurations studied. Those that failed to produce Moiré fringes of measurable contrast

(>0.5%) showed little to no emission at ~ 8 keV. In general, X-pinch emission from multiple sources and/or sources with large sizes produced low contrast or faint fringes. The Moiré

images with highest fringe contrast obtained with x-ray backlighting from each of the X-pinch configurations (Figure 5) are displayed in Figure 6.

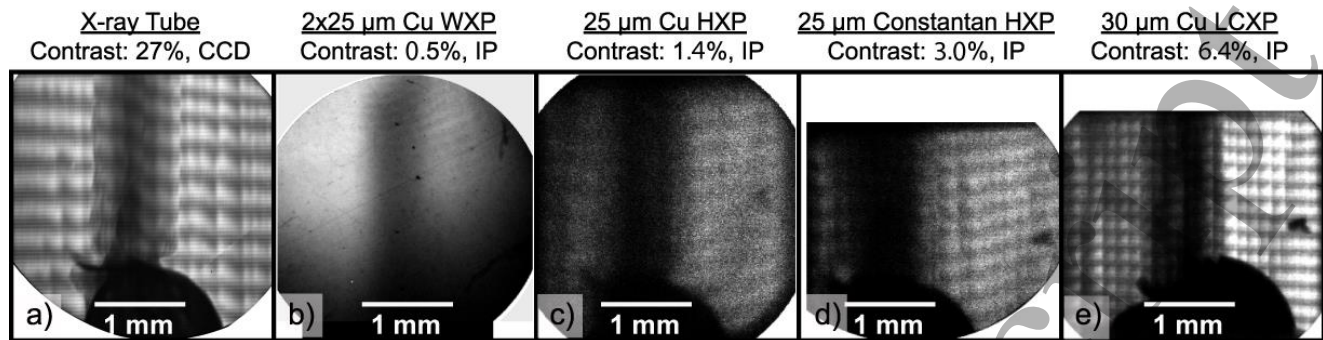


Figure 6. Moiré images of a static Be sheet set at an angle (as shown in Figure 1), from a) medical x-ray tube (Cu anode, 23 kV, 1 mA, 15 μm FWHM) with 27% contrast, b) 2x25 μm Cu WXP with 0.5% contrast, c) 25 μm Cu HXP with 1.4% contrast, d) 25 μm Constantan HXP with 3.0% contrast, and e) a 30 μm thick Cu LCXP with 6.4% contrast. Frame a) was recorded with an x-ray charge coupled device (CCD), which yields Moiré images with higher contrast than the image plate (IP) used for frames b-e. Contrast is given for each frame (note that the color contrast for the pictures above have been adjusted digitally for display purposes).

The ‘Static target’ TXD image obtained with 2x25 μm WXP backlighting is shown in Figure 6b. The Moiré fringe contrast in this image was 0.5%, much lower than the 27% contrast produced using a Cu x-ray tube source (Figure 6a). This lower contrast was expected (as discussed in the previous section), as well as the source size data (see red line, Figure 5b), likely driven by the long-lasting, high-flux electron beam (see red line, Figure 5a) lead to the poor resolving of fringes and the blurred edges of the static Be target.

Typical results from a 25 μm Cu HXP are shown in Figure 6c. A contrast of $\sim 1.4\%$ was measured and while fringes are clearly visible, the low flux of the Cu HXP resulted in limited penetration of x-rays through the target, making measuring the fringe shift (to obtain electron density) difficult. This was generally expected, given the low amount of hard x-ray flux seen in the maroon-colored line in Figure 5b. It is worth noting that in a few Cu HXP shots there were multiple co-located x-ray sources (inferred from penumbral data that did not show multiple shadows on any of the wires), separated by ~ 2 -10 ns. The increased x-ray flux from the multiple sources combined with their overlapping position produced much higher fringe contrast of 2.9% with fringes traceable through the Be target (adequate flux for penetration), but since these were not reproducible, their usefulness is limited.

Moiré data from the 25 μm Constantan HXPs are shown in Figure 6d, which produced fringe contrast of up to 3.0% with enough flux to partially penetrate the static Be target. However, the energy range of the emission spectrum (green line in Figure 5c ultimately appears to limit the overall usefulness of this setup. The differences in diffraction between the Ni and Cu K-shell lines appears to smear the edges of the Be target more than what is expected from a small (see the green line in Fig. 5b) hard x-ray source, especially when compared to the test image in Figure 6a).

From this data, it appears that further testing is needed to determine whether Cu HXPs can provide a useful 8 keV source for the TXD platform. Alternatively, using a higher Z material such as tantalum, whose L_{α} energy is very similar to the Cu K_{α} , may be a useful alternative.

A few variations were made to the Hybrid X-pinch configuration to optimize pinch timing and thus enhance x-ray emission from the hotspot. As mentioned previously, the conical electrode gap was found to be an important parameter affecting gap closure and therefore, pinch timing, and subsequent e-beam emission [76], [77]. Further details on hybrid X-pinch on GenASIS can be found in Ref. [31].

Figure 6e shows characteristic results from the laser-cut foil X-pinch, which as mentioned above produced the highest flux and smallest size hard x-ray sources of any configuration tested. From Figure 6e, it is clear that the LCXPs produce a superior x-ray backlighting source for the TXD diagnostic. The higher 8 keV flux (relative to the other configurations) leads to visible Moiré fringes through the static Be target, facilitating actual electron density measurements of said target (see Section 4.3), while the small source size clearly resolves both the edges of the Be target. Furthermore, the high spatial resolution achieved makes g_2 grating supporting structures visible, as observed previously [22]. Moiré fringe contrast from these targets ranged from 2.3-9.5%, at times achieving over 3 times the contrast produced by the other configurations.

Figure 7 further highlights the quality and reproducibility of the Moiré images obtained with x-ray emission from laser-cut X-pinch. The highest contrast from the selected LCXP images was measured at $6.4 \pm 0.2\%$ for 30 μm foil thickness (Figure 7a), and for 25 μm foil thickness $5.0 \pm 0.2\%$ and $4.2 \pm 1.2\%$ (Figures 7b and 7c), respectively. The fringe contrast corresponding to these Moiré images is plotted in Figure 7d. These results demonstrate that laser-cut X-pinch provide far

superior x-ray backlighting for 8 keV TXD diagnostics considering that, on average, the contrast measured almost doubles that of WXP and HXP configurations. Moreover, the small x-ray source ($<5 \mu\text{m}$) measured with radiographic diagnostics (shown in Figure 5b), provides spatial resolution that is beneficial for TXD phase retrieval techniques and increases accuracy when mapping electron density gradients.

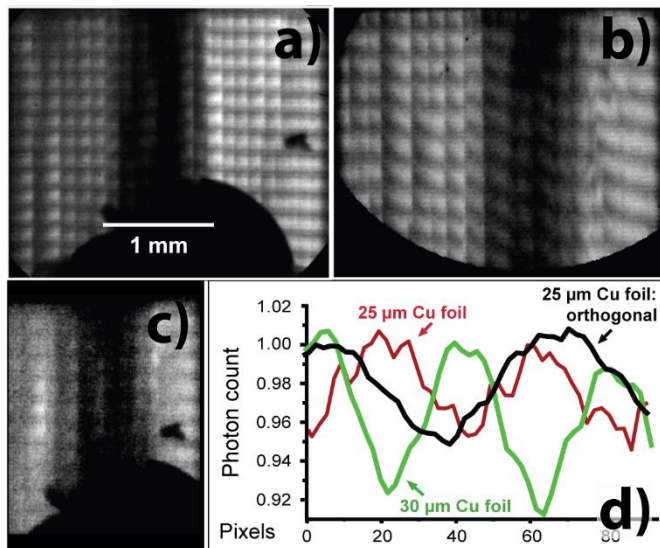


Figure 7. Moiré images of a Be sheet obtained with laser-cut X-pinch illumination from a) $30 \mu\text{m}$ with 6.4% contrast and b,c) $25 \mu\text{m}$ foil thickness with 5.0% and 4.2% contrast. a) and c) correspond to the same TXD platform used on different shots. b) and c) correspond to the same shot images with two separate and orthogonal TXD platforms. d) Normalized intensity lineouts used to determine Moiré fringe contrast (note that the color contrast for the pictures above have been adjusted digitally for display purposes).

It is worth noting that Figure 7b and c show Moiré images of a single $25 \mu\text{m}$ foil laser-cut X-pinch target, recorded using two separate and equivalent Talbot-Lau X-ray Deflectometers placed along the X-pinch cross-point to interferometer line-of-sight and orthogonal to one another. The comparable quality of fringe patterns retrieved for a single shot (Figure 7b and c), indicate that the source is – at least generally – symmetrical on the horizontal plane. It is worth noting that the brightness and contrast of the images have been modified in the figure to better showcase the different Moiré features. Figure 7c has a slightly lower photon count on the image plate, which might be due to the slight interferometer misalignment observed with respect to line-of-sight, justifying the error in fringe contrast measurements due to larger signal to noise ratio. Nevertheless, the LCXP Moiré images retrieved showcase the small shot-to-shot variation, considering Figure 7a and c, as well as the radial symmetry nature of laser-cut X-pinch emission, considering Figure 7b and c. The latter images also reveal a slight misalignment of the TXD platform, but the overall flux measured for both Moiré images is comparable,

thus it is demonstrated that small deviations from line-of-sight are not expected to impact Moiré fringe contrast significantly.

The results above demonstrate that Laser-cut X-pinch, driven by the GenASIS current driver, are the most suitable x-ray source for the specific TXD diagnostic system here presented. In particular, Moiré fringe LCXP fringe contrast exceeds that obtained using WXP and HXP. Moreover, the small x-ray source measured with radiographic diagnostics (Figure 5a) provides spatial resolution that is beneficial for TXD phase retrieval techniques which increases accuracy when mapping electron density gradients.

4.3 Electron density measurements

Laser-cut copper X-pinch generated Moiré images with high enough contrast to accurately measure Moiré fringe shifts. While the low photon count recorded on the image plates prevented phase retrieval through computational methods, single fringe tracking was performed to obtain fringe shift values. Average fringe shift values were used to retrieve electron density values. Moiré images of the beryllium sheet delivered a fringe shift of 0.29 ± 0.14 when using backlighting from a laser-cut X-pinch (Figure 7a). This matches the 0.29 ± 0.07 fringe shift measured using copper anode x-ray tube backlighting (Figure 6a). Similarly, fringe shifts of 0.43 ± 0.08 and 0.43 ± 0.02 were measured in the orthogonal direction from laser-cut X-pinch (Figure 7b) and medical x-ray tube backlighting, respectively. Recall that the fringe shift is proportional to the electron density gradient along the probing x-ray beam line-of-sight, hence it depends on object geometry and orientation. While the dimensions of the beryllium sheets imaged with both Talbot-Lau interferometers were the same, rotation angle was varied between Figure 7a and b, which changed the x-ray refraction angle (and fringe shift) in these images. The electron density retrieved from Figure 7a was $5.13 \pm 2.48 \times 10^{23} \text{ cm}^{-3}$, and converting to mass density, the value obtained was $1.92 \pm 0.97 \text{ g/cm}^3$, a 3.8% overestimation of the tabulated value for beryllium, which is well within the measurement uncertainty. Similarly, $5.16 \pm 0.96 \times 10^{23} \text{ cm}^{-3}$ electron density was measured from Figure 7b and $1.93 \pm 0.36 \text{ g/cm}^3$ mass density, representing a 4.5% overestimation. Note that fringe shift measurement errors presented are associated to spatial resolution limitations. These values were chosen over statistical errors as they are larger and better represent the limitations of the experimental diagnostic system in combination with x-ray backlighter source characteristics from each X-pinch configuration.

4.4 Plasma imaging through TXD

Once it was determined that $30 \mu\text{m}$ copper foil laser-cut X-pinch produced the most efficient x-ray backlighters for the 8 keV TXD interferometer here presented, the ‘Dynamic

target' platform was implemented to image a plasma target, maintaining the previously used grating periods and Talbot distances. Wire X-pinch loads were placed on the return current path of the GenASIS generator, along the line-of-sight of the x-ray backlighter (produced by a laser-cut X-pinch) and the interferometer, as done in Ref. [96]. The Moiré images recorded for three plasma loads are shown in Figure 8. It should be noted that these images are the first dynamic plasma objects imaged by a Talbot-Lau X-ray Deflectometer.

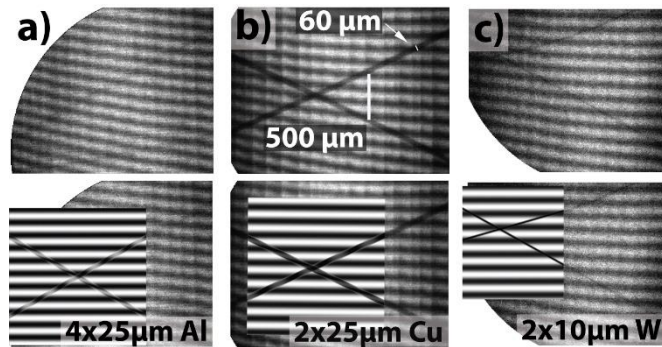


Figure 8. Talbot-Lau X-ray Deflectometry images for three X-pinch loads driven by GenASIS return current, backlit by 8 keV x-rays emitted from a 30 μm laser-cut X-pinch. a) 4x25 μm Al X-pinch with only one wire within field-of-view and contrast measured at 2.9%, b) 2x25 μm Cu X-pinch with 4.0% contrast, and c) 2x10 μm W X-pinch of 5.2% contrast where the return-current X-pinch were over-massed and so did not pinch. The experimental images (top) are compared to XWFP simulations overlapped to experimental images (bottom). *Note that the color contrast for the pictures above have been adjusted digitally for display purposes.

While the aluminum wire X-pinch image is too transparent, with a transmission of over 72%, the tungsten wire X-pinch is too attenuating, with a transmission of under 7%. Out of the three X-pinch loads shown above, the copper wire x-pinch seems to be the ideal candidate to be imaged on GenASIS using the present TXD platform, showing a transmission close to 32%. This configuration also shows fringe refraction caused by the expanded wires. Cu wire expansion was measured for each of the current return X-pinch wires at $58 \pm 2 \mu\text{m}$ and $59 \pm 3 \mu\text{m}$, representing an expansion of 2.3x at 126 ns after current start.

Fringe shift measurement within the wire core was not achieved at this time due to spatial resolution limitations. Even though the x-ray source size is small ($<5 \mu\text{m}$), object magnification is low and considering image plate resolution, absolute fringe shifts could not be determined precisely within the measurement error. Moreover, electron density gradients, as determined by simulated x-ray refraction angles, are high, making fringe shifts hard to track within the recorded Moiré image. Nevertheless, to evaluate and analyze the experimental Moiré images recorded, XWFP [80] simulations were performed considering wire size, material, and expansion. The experimental results agree with the simulated Moiré images, encouraging further investigation. In future experimental

activities, higher magnification will be used to increase spatial resolution as well as using x-ray film, which should also increase fringe contrast, as described above. Most importantly, a single Cu (or Constantan) wire of larger radius would be a better plasma object to image considering the TXD system restrictions in the current GenASIS configuration. These results allow for assessment of TXD platform scaling to larger pulsed-power generators. The adaptation to larger facilities enables diagnosing experiments relevant to Magnetic Liner Inertial Fusion, where the metallic liners are opaque to visible light but transparent to x-rays, thus TXD can provide high resolution electron density mapping.

5. Summary

Three types of X-pinch configurations – wire, hybrid, and laser-cut – were driven by the compact current driver GenASIS ($\sim 200 \text{ kA}$ current, 150 ns quarter-period). WXP, HXP, and LCXP made of copper, in addition to Constantan HXPs, were characterized and optimized as 8 keV sources for a Talbot-Lau X-ray Deflectometer to enable electron density diagnostics for HEDP experiments. The x-ray emission from the X-pinch configurations was characterized in terms of reproducibility, flux, timing, and source size considering the requirements of Talbot-Lau interferometry diagnostics.

Moiré Deflectometry images were recorded using x-ray backlighting obtained from each X-pinch configuration studied. Filtering enabled source and phase grating survival when imaging static solid and dynamic plasma loads. Moiré Deflectometry images were recorded using x-ray backlighting obtained from each X-pinch configuration studied. The image plates recorded fringe contrast of $<1\%$ for WXPs, $\sim 1\%$ and 3% for copper and Constantan HXPs respectively, and $\sim 4\text{-}6\%$ for LCXPs. Electron density from static solid Be samples was retrieved with $<5\%$ deviation from tabulated values using LXCP backlighting. These values reflect x-ray emission characteristics of each X-pinch configuration: while WXPs, HXPs, and LCXPs emit x-ray sources close to experimental temporal ($\sim 1\text{-}2 \text{ ns}$ FWHM) and spatial ($\sim 5 \mu\text{m}$) resolution limits, filtered diode and spectrometer data show increasing thermal x-ray flux, likely due to increasing source temperatures from HXPs to WXPs to LCXPs. While WXPs produced significant emission above 8 keV (outside the optimal interferometer contrast curve), it was from large ($>50 \mu\text{m}$), potential moving electron beams, resulting in double exposures. Cu HXP's produced small ($\sim 5 \mu\text{m}$) sources below 1 keV, more reliably than WXPs, with less emission above 3 keV. Constantan HXPs showed improved source parameters (duration, size, reproducibility), but the addition of nickel emission lines broadens the energy bandwidth to the detriment of electron density retrieval accuracy. LCXPs exhibited the highest single-source reproducibility and produced the highest

flux (almost twice as much as the other configurations) from the smallest 8 keV sources of all configurations.

Considering the above, LCXPs produced the best x-ray backlighter sources for TXD diagnostics in the pulsed-power environment using the 8 keV Talbot-Lau X-ray interferometer described in the above. X-ray spectral analysis and Moiré image quality evaluation of the ‘Static target’ encouraged TXD measurements of dynamic plasma objects produced by Al, Cu, and W X-pinch loads driven by the return current of GenASIS. Simulations indicate that 25 μm copper wire X-pinch produce fringe shifts within the expanded core, matching the Moiré images obtained experimentally. Wire expansion was measured although fringe shift tracking but limited by spatial and angular resolution.

X-ray flux from laser-cut X-pinch ($\sim 10^{10}$ photons/ns/sr) is sufficient to accurately retrieve fringe shift maps in the pulsed-power environment. The Moiré Deflectometry images recorded using x-ray backlighting from the X-pinch configurations studied demonstrate that TXD can be a powerful x-ray refraction-based imaging diagnostic for dense Z-pinch loads. It is worth noting that previous TXD diagnostic adaptations for HEDP experiments using laser-produced sources ($\sim 10^{11-13}$ photons/pulse/sr) require a monochromatic TXD configuration to achieve optimal Moiré fringe contrast. In contrast, copper X-pinch emission has little to no higher energy emission outside the interferometer design energy (8 keV), maximizing interferometer contrast and thus improving electron density retrieval accuracy.

Future studies will seek to diagnose dynamic plasma loads through Moiré imaging. The diagnostic spatial resolution and Moiré fringe contrast of the system described will be improved by modifying probed object size, geometry, and position relative to the gratings. Moreover, x-ray film is expected to improve Moiré fringe contrast, which combined with increased angular resolution, will allow for accurate fringe shift measurements. Considering the above, a compact (and perhaps portable) laser-cut x-pinch discharge could serve as x-ray backlighter source for a specially designed Talbot-Lau X-ray interferometer to enable attenuation, phase, scatter, and elemental composition diagnostics for MagLIF and other HED experiments through TXD diagnostics.

Acknowledgements

This material is based upon work supported by the Department of Energy, National Nuclear Security Administration under Award Numbers DE-NA0003882 and DE-NA0003842.

References

[1] E. I. Moses, R. N. Boyd, B. A. Remington, C. J. Keane, and R. Al-Ayat, “The National Ignition Facility: Ushering in a new age for high energy density science,” *Phys. Plasmas*, vol. 16, no. 4, 2009, doi: 10.1063/1.3116505.

- [2] A. Morace et al., “Development of x-ray radiography for high energy density physics,” *Phys. Plasmas*, vol. 21, no. 10, 2014, doi: 10.1063/1.4900867.
- [3] T. A. Shelkovenko, D. B. Sinars, S. A. Pikuz, K. M. Chandler, and D. A. Hammer, “Point-projection x-ray radiography using an X pinch as the radiation source,” *Rev. Sci. Instrum.*, vol. 72, no. 1 II, pp. 667–670, 2001, doi: 10.1063/1.1323252.
- [4] J. D. Douglass and D. A. Hammer, “COBRA-STAR, a five frame point-projection x-ray imaging system for 1 MA scale wire-array Z pinches,” *Rev. Sci. Instrum.*, vol. 79, no. 3, p. 033503, Mar. 2008, doi: 10.1063/1.2884707.
- [5] K. S. Raman et al., “An in-flight radiography platform to measure hydrodynamic instability growth in inertial confinement fusion capsules at the National Ignition Facility,” *Phys. Plasmas*, vol. 21, no. 7, 2014, doi: 10.1063/1.4890570.
- [6] A. Ravasio et al., “Hard x-ray radiography for density measurement in shock compressed matter,” *Phys. Plasmas*, vol. 15, no. 6, pp. 3–6, 2008, doi: 10.1063/1.2928156.
- [7] R. Tommasini et al., “Development of backlighting sources for a Compton radiography diagnostic of inertial confinement fusion targets,” *Rev. Sci. Instrum.*, vol. 79, no. 10, pp. 1–5, 2008, doi: 10.1063/1.2953593.
- [8] S. A. Slutz and R. A. Vesey, “High-gain magnetized inertial fusion,” *Phys. Rev. Lett.*, vol. 108, no. 2, pp. 1–5, 2012, doi: 10.1103/PhysRevLett.108.025003.
- [9] R. D. McBride, M. R. Martin, R. W. Lemke, J. B. Greenly, and C. A. Jennings, “Beryllium liner implosion experiments on the Z accelerator in preparation for magnetized liner inertial fusion for magnetized liner inertial fusion a),” *Phys. Plasmas*, vol. 20, no. 056309, p. 056309, 2013, doi: 10.1063/1.4803079.
- [10] T. A. Shelkovenko et al., “Accelerated electrons and hard X-ray emission from X-pinch,” *Plasma Phys. Reports*, vol. 34, no. 9, pp. 754–770, 2008, doi: 10.1134/S1063780X08090109.
- [11] T. A. Shelkovenko, S. A. Pikuz, and D. A. Hammer, “A Review of Projection Radiography of Plasma and Biological Objects in X-Pinch Radiation,” *Plasma Phys. Reports*, vol. 42, no. 3, pp. 226–268, 2016, doi: 10.1134/S1063780X16030065.
- [12] S. A. Pikuz et al., “High-luminosity monochromatic x-ray backlighting using an incoherent plasma source to study extremely dense plasmas (invited),” *Rev. Sci. Instrum.*, vol. 68, no. 1, p. 740, 1997, doi: 10.1063/1.1147689.
- [13] O. L. Landen et al., “X-ray backlighting for the National Ignition Facility (invited),” *Rev. Sci. Instrum.*, vol. 72, no. 1 II, pp. 627–634, 2001, doi: 10.1063/1.1315641.
- [14] D. K. Bradley, O. L. Landen, A. B. Bullock, S. G. Glendinning, and R. E. Turner, “Efficient, 1–100-keV x-ray radiography with high spatial and temporal resolution,” *Opt. Lett.*, vol. 27, no. 2, p. 134, 2002, doi: 10.1364/ol.27.000134.
- [15] L. A. Pickworth et al., “A Kirkpatrick-Baez microscope for the national ignition facility,” *Rev. Sci. Instrum.*, vol. 85, no. 11, pp. 2014–2017, 2014, doi: 10.1063/1.4886433.
- [16] P. Kirkpatrick and A. V. Baez, “Formation of optical images by X-rays,” *J. Opt. Soc. Am.*, vol. 38, no. 1895, pp. 766–774, 1948, doi: 10.1364/JOSA.38.000766.
- [17] A. Do et al., “Fresnel zone plate development for x-ray radiography of hydrodynamic instabilities at the National Ignition Facility,” *Appl. Opt.*, vol. 59, no. 34, p. 10777, 2020, doi: 10.1364/ao.408569.
- [18] F. J. Marshall, “High-resolution x-ray radiography with Fresnel zone plates on the University of Rochester’s OMEGA Laser

- Systems,” *Rev. Sci. Instrum.*, vol. 92, no. October, p. 033701, 2021, doi: 10.1063/5.0034903.
- [19] C. Stoeckl et al., “A spherical crystal imager for OMEGA EP,” *Rev. Sci. Instrum.*, vol. 83, no. 3, 2012, doi: 10.1063/1.3693348.
- [20] M. S. Schollmeier et al., “A 7.2 keV spherical x-ray crystal backlighter for two-frame, two-color backlighting at Sandia’s Z Pulsed Power Facility,” *Rev. Sci. Instrum.*, vol. 88, no. 10, 2017, doi: 10.1063/1.4994566.
- [21] M. P. Valdivia et al., “Talbot-Lau X-ray Deflectometer: Refraction-based HEDP imaging diagnostic,” *Rev. Sci. Instrum.*, vol. 92, no. Proceedings of the 23rd Topical Conference on High-Temperature Plasma Diagnostics, p. 065110, 2021, doi: 10.1063/5.0043655.
- [22] M. P. Valdivia, D. Stutman, and M. Finkenthal, “Moire deflectometry using the Talbot-Lau interferometer as refraction diagnostic for High Energy Density plasmas at energies below 10 keV,” *Rev. Sci. Instrum.*, vol. 85, no. 7, p. 073702, 2014, doi: 10.1063/1.4885467.
- [23] M. P. Valdivia, D. Stutman, and M. Finkenthal, “Single-shot Z eff dense plasma diagnostic through simultaneous refraction and attenuation measurements with a Talbot – Lau x-ray moiré deflectometer,” *Appl Opt.*, vol. 54, no. 10, pp. 2577–2583, 2015, doi: 10.1364/AO.54.002577.
- [24] W. Yashiro, Y. Terui, K. Kawabata, and A. Momose, “On the origin of visibility contrast in x-ray Talbot interferometry,” vol. 18, no. 16, pp. 16890–16901, 2010.
- [25] G. Chen, N. Bevins, J. Zambelli, and Z. Qi, “Small-angle scattering computed tomography (SAS-CT) using a Talbot-Lau interferometer and a rotating anode x-ray tube : theory and experiments,” vol. 18, no. 12, pp. 2747–2753, 2010.
- [26] K. Yasuike, M. H. Key, S. P. Hatchett, R. A. Snavely, and K. B. Wharton, “Hot electron diagnostic in a solid laser target by K - shell lines measurement from ultraintense laser – plasma interactions,” *Rev. Sci. Instrum.*, vol. 72, p. 1236, 2006, doi: 10.1063/1.1319373.
- [27] K. Wharton et al., “Experimental Measurements of Hot Electrons Generated by Ultraintense (>10¹⁹ W/cm²) Laser-Plasma Interactions on Solid-Density Targets,” *Phys. Rev. Lett.*, vol. 81, no. 4, pp. 822–825, 1998, doi: 10.1103/PhysRevLett.81.822.
- [28] D. Matthews et al., “Characterization of laser-produced plasma x-ray sources for use in x-ray radiography,” *J. Appl. Phys.*, vol. 54, no. 1983, p. 4260, 1983, [Online]. Available: <http://link.aip.org/link/?JAPIAU/54/4260/1>.
- [29] A. Rousse et al., “Efficient K x-ray source from femtosecond laser-produced plasmas,” *Phys. Rev. E*, vol. 50, no. 3, pp. 2200–2207, 1994, doi: 10.1103/PhysRevE.50.2200.
- [30] F. N. Beg et al., “A study of picosecond laser–solid interactions up to 10¹⁹ W cm^{−2},” *Phys. Plasmas*, vol. 4, no. 2, pp. 447–457, 1997, doi: 10.1063/1.872103.
- [31] G. W. Collins et al., “Direct comparison of wire, foil, and hybrid X-pinch on a 200 kA, 150 ns current driver,” *J. Appl. Phys.*, vol. 129, no. 7, 2021, doi: 10.1063/5.0035587.
- [32] M. G. Haines, “A review of the dense Z -pinch,” *Plasma Phys. Control. Fusion*, vol. 53, no. 9, p. 093001, 2011, doi: 10.1088/0741-3335/53/9/093001.
- [33] S. A. Pikuz, T. A. Shelkovenko, and D. A. Hammer, “X-pinch. Part I,” *Plasma Phys. Reports*, vol. 41, no. 4, pp. 291–342, 2015, doi: 10.1134/S1063780X15040054.
- [34] S. A. Pikuz, T. A. Shelkovenko, and D. A. Hammer, “X-pinch. Part II,” *Plasma Phys. Reports*, vol. 41, no. 6, pp. 445–491, 2015, doi: 10.1134/S1063780X15060045.
- [35] M. P. Valdivia et al., “X-ray backlighter requirements for refraction-based electron density diagnostics through Talbot-Lau deflectometry,” *Rev. Sci. Instrum.*, vol. 89, no. 10G127, pp. 138–145, 2018, doi: 10.1063/1.5039342.
- [36] F. N. Beg et al., “Compact X-pinch based point x-ray source for phase contrast imaging of inertial confinement fusion capsules,” *Appl. Phys. Lett.*, vol. 89, no. 10, p. 101502, 2006, doi: 10.1063/1.2335959.
- [37] R. V. Shapovalov, R. B. Spielman, and G. R. Imel, “An oil-free compact X-pinch plasma radiation source: Design and radiation performance,” *Rev. Sci. Instrum.*, vol. 88, no. 6, 2017, doi: 10.1063/1.4986460.
- [38] T. A. Shelkovenko et al., “X-pinch X-ray emission on a portable low-current, fast rise-time generator,” *J. Appl. Phys.*, vol. 124, no. 8, pp. 1–8, 2018, doi: 10.1063/1.5032112.
- [39] D. H. Kalantar and D. A. Hammer, “The x-pinch as a point source of x rays for backlighting,” *Rev. Sci. Instrum.*, vol. 66, no. 1, pp. 779–781, 1995, doi: 10.1063/1.1146219.
- [40] D. B. Sinars, S. A. Pikuz, T. A. Shelkovenko, K. M. Chandler, D. A. Hammer, and J. P. Apruzese, “Time-resolved spectroscopy of Al, Ti, and Mo X pinch radiation using an X-ray streak camera,” *J. Quant. Spectrosc. Radiat. Transf.*, vol. 78, no. 1, pp. 61–83, 2003, doi: 10.1016/S0022-4073(02)00180-2.
- [41] G. V. Ivanenkov, A. R. Mingaleev, S. A. Pikuz, V. M. Romanova, and S. Tatiana, “Experimental study of X-pinch dynamics,” no. May 1996, 2017.
- [42] M. Engelhardt et al., “The fractional Talbot effect in differential x-ray phase-contrast imaging for extended and polychromatic x-ray sources,” *J. Microsc.*, vol. 232, no. 1, pp. 145–157, 2008, doi: 10.1111/j.1365-2818.2008.02072.x.
- [43] A. Momose, S. Kawamoto, I. Koyama, Y. Hamaishi, K. Takai, and Y. Suzuki, “Demonstration of x-ray Talbot interferometry,” *Japanese J. Appl. Physics, Part 2 Lett.*, vol. 42, no. 7 B, 2003, doi: 10.1143/JJAP.42.L866.
- [44] F. Pfeiffer, T. Weitkamp, O. Bunk, and C. David, “Phase retrieval and differential phase-contrast imaging with low-brilliance X-ray sources,” *Nat. Phys.*, vol. 2, no. 4, pp. 258–261, Mar. 2006, doi: 10.1038/nphys265.
- [45] N. Bevins, J. Zambelli, K. Li, Z. Qi, and G.-H. Chen, “Multicontrast x-ray computed tomography imaging using Talbot-Lau interferometry without phase stepping,” *Med. Phys.*, vol. 39, no. 1, p. 424, 2012, doi: 10.1118/1.3672163.
- [46] Y. Takeda, W. Yashiro, T. Hattori, A. Takeuchi, Y. Suzuki, and A. Momose, “Differential phase X-ray imaging microscopy with X-ray talbot interferometer,” *Appl. Phys. Express*, vol. 1, no. 11, pp. 1170021–1170023, 2008, doi: 10.1143/APEX.1.117002.
- [47] E. E. Bennett, R. Kopace, A. F. Stein, and H. Wen, “A grating-based single-shot x-ray phase contrast and diffraction method for in vivo imaging,” *Med. Phys.*, vol. 37, no. 11, p. 6047, 2010, doi: 10.1118/1.3501311.
- [48] A. Momose et al., “Phase tomography by X-ray talbot interferometry for biological imaging,” *Japanese J. Appl. Physics, Part 1 Regul. Pap. Short Notes Rev. Pap.*, vol. 45, no. 6 A, pp. 5254–5262, 2006, doi: 10.1143/JJAP.45.5254.
- [49] T. Weitkamp et al., “Tomography with grating interferometers at low-brilliance sources,” no. 6318, pp. 1–10, 2006.

- [50] S. Bachche et al., "Laboratory-based X-ray phase-imaging scanner using Talbot-Lau interferometer for non-destructive testing," *Sci. Rep.*, vol. 7, no. 1, pp. 3–9, 2017, doi: 10.1038/s41598-017-07032-y.
- [51] W. Yashiro, S. Harasse, K. Kawabata, H. Kuwabara, T. Yamazaki, and A. Momose, "Distribution of unresolvable anisotropic microstructures revealed in visibility-contrast images using x-ray Talbot interferometry," *Phys. Rev. B - Condens. Matter Phys.*, vol. 84, no. 9, pp. 1–9, 2011, doi: 10.1103/PhysRevB.84.094106.
- [52] D. Ress et al., "Measurement of Laser-Plasma Electron Density with a Soft X-ray Laser Deflectometer.," *Science*, vol. 265, no. 5171, pp. 514–517, 1994, doi: 10.1126/science.265.5171.514.
- [53] B. Moosman, V. M. Bystritskii, C. J. Boswell, and F. J. Wessel, "Moiré deflectometry diagnostic for transient plasma, using a multipulse N2 laser," *Rev. Sci. Instrum.*, vol. 67, no. 1, p. 170, 1996, doi: 10.1063/1.1146566.
- [54] J. Ruiz-Camacho, F. N. Beg, and P. Lee, "Comparison of sensitivities of Moiré deflectometry and interferometry to measure electron densities in z -pinch plasmas," *J. Phys. D. Appl. Phys.*, vol. 40, no. 7, pp. 2026–2032, 2007, doi: 10.1088/0022-3727/40/7/026.
- [55] O. Kafri and I. Glatt, "Moiré Deflectometry: A Ray Deflection Approach To Optical Testing," *Opt. Eng.*, vol. 24, no. 6, p. 246944, 1985, doi: <https://doi.org/10.1117/12.7973607>.
- [56] L. Liu, "Partially coherent diffraction effect between Lau and Talbot effects," *J. Opt. Soc. Am. A*, vol. 5, no. 10, p. 1709, 1988, doi: 10.1364/josaa.5.001709.
- [57] J. Jahns and A. W. Lohmann, "The Lau effect (a diffraction experiment with incoherent illumination)," *Opt. Commun.*, vol. 28, no. 3, pp. 263–267, 1979, doi: 10.1016/0030-4018(79)90316-X.
- [58] G. J. Swanson and E. N. Leith, "Analysis of the Lau effect and generalized grating imaging," *J. Opt. Soc. Am. A*, vol. 2, no. 6, p. 789, 1985, doi: 10.1364/JOSAA.2.000789.
- [59] K. Patorski, "Incoherent Superposition of Multiple Self-imaging Lau Effect and Moiré Fringe Explanation," *Opt. Acta Int. J. Opt.*, vol. 30, no. 6, pp. 745–758, 2010, doi: 10.1080/713821267.
- [60] G. Sato et al., "Two-dimensional gratings-based phase-contrast imaging using a conventional x-ray tube.," *Opt. Lett.*, vol. 36, no. 18, pp. 3551–3, Sep. 2011, [Online]. Available: <http://www.ncbi.nlm.nih.gov/pubmed/21931387>.
- [61] M. P. Valdivia, D. Stutman, and M. Finkenthal, "Talbot-Lau based Moiré deflectometry with non-coherent sources as potential High Energy Density plasma diagnostic," *J. Appl. Phys.*, vol. 114, no. 16, p. 163302, 2013, doi: 10.1063/1.4827186.
- [62] D. Stutman and M. Finkenthal, "Talbot-Lau x-ray interferometry for high energy density plasma diagnostic.," *Rev. Sci. Instrum.*, vol. 82, no. 11, p. 113508, Nov. 2011, doi: 10.1063/1.3660808.
- [63] T. Donath et al., "Inverse geometry for grating-based x-ray phase-contrast imaging," *J. Appl. Phys.*, vol. 106, no. 5, pp. 2049–2064, 2009, doi: 10.1063/1.3208052.
- [64] M. P. Valdivia et al., "Talbot – Lau x-ray deflectometry phase-retrieval methods for electron density diagnostics in high-energy density experiments," *Appl. Opt.*, vol. 57, no. 2, pp. 13–15, 2018.
- [65] M. Vescovi, M. P. Valdivia, F. Veloso, D. Stutman, and M. Favre, "Implementation of Talbot–Lau x-ray deflectometry in the pulsed power environment using a copper X-pinch backlighter," *J. Appl. Phys.*, vol. 127, no. 20, p. 203301, 2020, doi: 10.1063/5.0001910.
- [66] M. P. Valdivia et al., "An x-ray backlit Talbot-Lau deflectometer for high-energy-density electron density diagnostics," *Rev. Sci. Instrum.*, vol. 87, no. 2, p. 023505, 2016, doi: 10.1063/1.4941441.
- [67] E. Brambrink et al., "Short-pulse laser-driven x-ray radiography," *High Power Laser Sci. Eng.*, vol. 4, no. 2016, p. e30, 2016, doi: 10.1017/hpl.2016.31.
- [68] A. Y. Faenov et al., "Advanced high resolution x-ray diagnostic for HEDP experiments," *Sci. Rep.*, vol. 8, no. 1, pp. 1–9, 2018, doi: 10.1038/s41598-018-34717-9.
- [69] S. C. Bott et al., "Ablation Studies of Low-Number Wire Arrays at 200 kA Using A Linear Transformer Driver," *IEEE Trans. Plasma Sci.*, vol. 38, no. 4, pp. 567–573, Apr. 2010, doi: 10.1109/TPS.2009.2034166.
- [70] R. Bott, S. Haas, D. Madden, R. Ueda, U. Eshaq, Y. Collins, G. Gunasekera, K. Mariscal, D. Peebles, J. Beg, F. Mazarakis, M. Struve, K. Sharpe, "250 kA compact linear transformer driver for wire array z-pinch loads," *Phys. Rev. Spec. Top. - Accel. Beams*, vol. 14, no. 5, pp. 1–8, May 2011, doi: 10.1103/PhysRevSTAB.14.050401.
- [71] S. V. Lebedev et al., "X-ray backlighting of wire array Z-pinch implosions using X pinch," *Rev. Sci. Instrum.*, vol. 72, no. 1, p. 671, 2001, doi: 10.1063/1.1315647.
- [72] V. V. Alexandrov et al., "Experimental study of wire array implosion in presence of prolonged plasma production on Angara-5-1 facility," *BEAMS 2002 - 14th Int. Conf. High-Power Part. Beams*, vol. 2, no. 2, pp. 91–94, 2002, doi: 10.1063/1.1531288.
- [73] J. Wu et al., "Experimental investigations of X-pinch backlighters on QiangGuang-1 generator," *Laser Part. Beams*, vol. 29, no. 2, pp. 155–160, 2011, doi: 10.1017/S0263034611000024.
- [74] J. D. Douglass, J. B. Greenly, D. A. Hammer, R. D. McBride, and S. A. Pikuz, "The Imaging of Z-Pinches Using X- Pinch Backlighting The Imaging of Z-Pinches Using X-Pinch," vol. 129, no. December 2005, 2016.
- [75] F. N. Beg et al., "Table-top X-pinch for x-ray radiography," *Appl. Phys. Lett.*, vol. 82, no. 25, p. 4602, 2003, doi: 10.1063/1.1584782.
- [76] T. A. Shelkovenko et al., "Hybrid X-pinch with conical electrodes," *Phys. Plasmas*, vol. 17, no. 11, p. 112707, 2010, doi: 10.1063/1.3504226.
- [77] T. A. Shelkovenko et al., "Dynamics of hybrid X-pinches," *Plasma Phys. Reports*, vol. 41, no. 1, pp. 52–70, 2015, doi: 10.1134/S1063780X15010031.
- [78] G. W. Collins et al., "Investigation into the dynamics of laser-cut foil X-pinches and their potential use for high repetition rate operation," *Appl. Phys. Lett.*, vol. 105, no. 2, p. 024101, 2014, doi: 10.1063/1.4889748.
- [79] G. W. Collins et al., "Characterization of laser-cut copper foil X-pinches," *Phys. Plasmas*, vol. 23, no. 10, p. 101212, 2016, doi: 10.1063/1.4965238.
- [80] T. Weitkamp, "XWFP: an x-ray wavefront propagation software package for the IDL computer language," *Adv.*

- Comput. Methods X-Ray Neutron Opt., vol. 5536, no. October 2004, pp. 181–189, 2004, doi: 10.1117/12.569642.
- [81] A. R. Mingaleev et al., “Spectra of multiply charged nickel and copper ions in an X-pinch plasma,” *Quantum Electron.*, vol. 23, no. 5, pp. 397–405, 1993, doi: 10.1070/qe1993v023n05abeh003061.
- [82] S. Zakharov, G. Ivanenkov, A. Kolomenskii, S. Pikuz, A. Samokhin, and I. Ulshmid, “Wire x-pinch in a high-current diode,” *Sov. Tech. Phys. Lett.*, vol. 8, pp. 456–457, 1982.
- [83] “Opto Diode Corporation.”
- [84] P. A. Ross, “A New Method of Spectroscopy for Faint X-Radiations,” *J. Opt. Soc. Am.*, vol. 16, no. 6, p. 433, 1928, doi: 10.1364/josa.16.000433.
- [85] H. Legall, H. Stiel, V. Arkadiev, and A. A. Bjeoumikhov, “High spectral resolution x-ray optics with highly oriented pyrolytic graphite,” *Opt. Express*, vol. 14, no. 10, p. 4570, 2006, doi: 10.1364/oe.14.004570.
- [86] P. Choi, C. Dumitrescu, E. Wyndham, M. Favre, and H. Chuaqui, “Slit-wire camera, a new diagnostics method for measurement of small scale high-energy density structures in hot plasmas,” *Rev. Sci. Instrum.*, vol. 73, no. 6, p. 2276, 2002, doi: 10.1063/1.1480462.
- [87] T. A. Shelkovenko, S. A. Pikuz, D. A. Hammer, Y. S. Dimant, and A. R. Mingaleev, “Evolution of the structure of the dense plasma near the cross point in exploding wire x pinches,” *Phys. Plasmas*, vol. 6, pp. 2840–2846, 1999, doi: <https://doi.org/10.1063/1.873241>.
- [88] H. Chen et al., “Absolute calibration of image plates for electrons at energy between 100 keV and 4 MeV,” *Rev. Sci. Instrum.*, vol. 79, no. 3, pp. 3–6, 2008, doi: 10.1063/1.2885045.
- [89] M. J. Haugh, J. Lee, E. Romano, and M. Schneider, “Calibrating image plate sensitivity in the 700 to 5000 eV spectral energy range,” *Target Diagnostics Phys. Eng. Inert. Confin. Fusion II*, vol. 8850, no. September 2013, p. 885007, 2013, doi: 10.1117/12.2024889.
- [90] K. M. Chandler et al., “Cross calibration of new x-ray films against direct exposure film from 1 to 8 keV using the X-pinch x-ray source Cross calibration of new x-ray films against direct exposure film from 1 to 8 keV using the X-pinch x-ray source,” *Rev. Sci. Instrum.*, vol. 76, no. 2005, p. 113111, 2006, doi: 10.1063/1.2135276.
- [91] G. A. Kyrala, “Cross calibration of AGFA-D7 x-ray film against direct exposure film from using laser generated x-rays from 2 to 8.5 keV using laser generated x-rays,” *Rev. Sci. Instrum.*, vol. 77, no. 5, p. 055104, 2006, doi: 10.1063/1.2194787.
- [92] N. E. Lanier, J. S. Cowan, and J. Workman, “Characterization and cross calibration of Agfa D4, D7, and D8 and Kodak SR45 x-ray films against direct exposure film at 4.0 – 5.5 keV,” *Rev. Sci. Instrum.*, vol. 77, p. 043504, 2006, doi: 10.1063/1.2194509.
- [93] J. P. Knauer et al., “Response model for Kodak Biomax-MS film,” *Rev. Sci. Instrum.*, vol. 77, no. October, p. 10F331, 2006, doi: 10.1063/1.2220046.
- [94] F. J. Marshall, J. P. Knauer, D. Anderson, and B. L. Schmitt, “Absolute calibration of Kodak Biomax-MS film response to x rays in the 1.5- to 8-keV energy range,” *Rev. Sci. Instrum.*, vol. 77, no. 10, p. 10F308, 2006, doi: 10.1063/1.2221698.
- [95] J. P. Holder et al., “On the system stability and calibration of the image plate/scanner system for plasma diagnosis at the National Ignition Facility,” *Rev. Sci. Instrum.*, vol. 89, no. 10, 2018, doi: 10.1063/1.5039363.
- [96] D. H. Kalantar and D. A. Hammer, “Observation of a stable dense core within an unstable coronal plasma in wire-initiated dense Z-pinch experiments,” *Phys. Rev. Lett.*, vol. 71, no. 23, pp. 3806–3809, 1993, doi: 10.1103/PhysRevLett.71.3806.